https://doi.org/10.5194/egusphere-2026-2017
Preprint. Discussion started: 29 April 2026

Enhanced discrimination of vertical aerosol types based on multi-wavelength Mie-Raman-fluorescence lidar at a high-altitude background site

Yutong Tian [1,2], Ting Yang[1*], Zifa Wang[1,2], Linghan Zeng[1], Yining Tan[1,2], Weichun Liang[3], Qingqing Xia[3], Tong Wang[4], Shitian Kou[5]

[1]State Key Laboratory of Atmospheric Environment and Extreme Meteorology, Institute of Atmospheric Physics, Chinese Academy of Sciences, Beijing, 100029, China
[2]College of Earth and Planetary Sciences, University of Chinese Academy of Sciences, Beijing, 100049, China
[3]Wuxi CAS Photonics Co., Ltd., Wuxi, 214135, China
[4]Qingdao Junray Intelligent Instrument Co.,Ltd., Qingdao, 266000, China
[5]Shandong Qianzhi Technology Co., Ltd., Jinan, 250000, China

Correspondence to: Ting Yang (tingyang@mail.iap.ac.cn)

Abstract. Accurate classification of the vertical distribution of tropospheric aerosols is critical for reducing uncertainties in climate effect assessments. To address the challenge of aerosol classification uncertainties inherent in traditional lidar retrievals under complex mixed scenarios, this study leverages the unique locational advantage of the Atmospheric Boundary Layer Eco-Environment Shanghuang Observatory (ABLES) to develop an advanced synergistic retrieval algorithm based on a multi-wavelength Mie-Raman-fluorescence lidar system. The proposed scheme establishes a seven-parameter synergistic constraint, integrating fluorescence capacity, particle depolarization ratios (*PDR*), backscatter-related Ångström exponents (*BÅE*), and lidar ratios (*LR*). By combining Monte Carlo simulations with least squares minimization, the algorithm achieves a quantitative decomposition of scattering contribution fractions for smoke, urban, pollen, and dust. A key advantage is the robust physical constraint system, which ensures classification relies on intrinsic microphysical properties rather than signal intensity alone, thereby avoiding biases from backscatter anomalies. Multi-platform cross-validation confirms the high reliability of the algorithm across a wide dynamic range, with the coefficient of determination between near-surface retrieval results and in situ monitoring data exceeding 0.6. Furthermore, sensitivity analysis indicates that the multi-parameter scheme effectively captures the differential microphysical responses of aerosols across seasons and altitudes. This physically decouples meteorologically driven optical enhancement from actual mass concentration fluctuations, providing strong technical support for high-precision, high-spatiotemporal-resolution aerosol typing and mass retrieval at high-altitude background stations.

1 Introduction

Atmospheric aerosols serve as some of the most active and spatiotemporally variable components within the system of the Earth and the atmosphere. They directly modulate the energy budget of the Earth through radiative forcing and indirectly influence the water cycle by modifying cloud microphysical processes (Akinyoola et al., 2024; Levy Ii et al., 2013; Wang,

https://doi.org/10.5194/egusphere-2026-2017
Preprint. Discussion started: 29 April 2026

2025). However, significant uncertainties remain regarding their quantification in climate models (Quaas et al., 2020; Li et al., 2022). In the troposphere, aerosols from diverse sources with varying physical properties exhibit a highly inhomogeneous vertical distribution, with chemical composition, morphology, and optical properties changing rapidly with height (Chen et al., 2023; Gui et al., 2022). Consequently, vertically resolved observations of four typical aerosol types, namely smoke, urban, pollen, and dust, are crucial for resolving tropospheric dynamic processes.

Specifically, the injection height of smoke aerosols, particularly those from biomass burning and wildfires, determines the atmospheric lifetime and transport range of the particles (Pan et al., 2026). Particles within elevated smoke layers may also serve as ice nuclei or cloud condensation nuclei, thereby modulating precipitation and the response of clouds to radiation (Peterson et al., 2018; Yu et al., 2019). Urban aerosols are primarily distributed within the planetary boundary layer and are governed by the interaction between anthropogenic emissions and meteorological conditions (Rajesh and Ramachandran, 2020; Ahmad et al., 2025). Their composition, which contains anthropogenic inorganic salts and secondary organic aerosols, significantly impacts the hygroscopic growth of the particles, thus altering the visibility and optical depth of the urban atmosphere (Young et al., 2022). Mineral dust is one of the natural aerosols with the largest mass load. Aside from influencing marine biogeochemical cycles via deposition, the distinct nonspherical nature of dust is a key factor in the assessment of radiative cooling effects (Ito et al., 2021). Frequently lifted by convection and large-scale circulation, these particles possess the capacity for long-range intercontinental transport. As a bioaerosol, pollen is characterized by relatively large particle size and complex morphology. Its vertical distribution reflects biological emission, turbulent mixing, and deposition. Furthermore, submicron fragments released during rupture at specific humidity levels act as efficient ice nuclei and play a non-negligible role in the formation of mixed-phase clouds (Matthews et al., 2023; Prank et al., 2025). Therefore, the accurate identification of these four aerosol types and the retrieval of their mass concentrations are prerequisites for deconstructing regional climate effects.

When quantitatively characterizing the vertical structure of the aerosol, macroscopic optical parameters serve as a crucial link connecting remote sensing observations with the complex nonlinear mapping relationships of aerosol microphysical characteristics, such as morphology, size, and refractive index. Specifically, the particle depolarization ratios (*PDR*) at 355 and 532 nm provide key information on particle nonsphericity. The spectral difference between the two directly reflects the size parameter characteristics of nonspherical particles, which is critical for distinguishing coarse-mode mineral dust from certain pollen types or aged smoke aggregates possessing specific microstructures (Haarig et al., 2022). Fluorescence is a diagnostic bio-fingerprint for atmospheric particles. The fluorescence capacity (G_F) provides complementary information to depolarization ratios and enables discrimination between pollen and mineral dust under low-*PDR* conditions (Veselovskii et al., 2024). Simultaneously, the extinction-to-backscatter ratios, also known as lidar ratios (*LR*), at 355 and 532 nm contain information on particle size distribution and complex refractive index (Schuster et al., 2012). These are essential quantities for distinguishing absorbing smoke, non-absorbing fine sulfate aerosol, and coarse-mode dust (Haarig et al., 2025). The backscatter-related Ångström exponent (*BÅE*) between different wavelengths, which characterizes the dependence of the backscatter coefficient on wavelength, reflects the spectral sensitivity of the aerosol size distribution and provides a means of

https://doi.org/10.5194/egusphere-2026-2017
Preprint. Discussion started: 29 April 2026

separating coarse-mode and fine-mode particles (Wang et al., 2022). In summary, the synergistic evolution of these multidimensional macroscopic optical parameters in vertical space provides indispensable physical constraints for precisely analyzing the distribution patterns and dynamic evolution mechanisms of different aerosol types within the troposphere.

The acquisition of such a comprehensive set of optical data with high fidelity relies on breakthroughs in remote sensing techniques from the ground. Multiwavelength Mie–Raman–fluorescence lidar systems have become cutting-edge tools for atmospheric profiling. By combining multiwavelength Mie and Raman measurements with highly sensitive fluorescence detection, such systems can capture aerosol hygroscopic growth and external mixing processes at high spatiotemporal resolution (Miri et al., 2024; Jiang et al., 2024), and simultaneously identify aerosols containing biological or organic components (Veselovskii et al., 2022). Recent observations indicate that such systems possess unique advantages in detecting invisible aerosol layers with low optical depth, making them particularly suitable for studying high-altitude transported smoke, pollen, and complex aerosol mixtures (Veselovskii et al., 2023; Gast et al., 2025), as well as realizing the identification and quantification of humic-like substances (Huang et al., 2025). However, while advanced lidar systems provide rich observational data, the joint application of such data remains limited in current research. Most algorithms employ only a limited subset of parameters and fail to fully utilize the complete set of macroscopic optical parameters, including the backscatter coefficient (β), *LR*, *PDR*, G_F, and *BÅE*, to create more reliable aerosol classification algorithms.

This study proposes an improved multiparameter inversion method for quantifying aerosol components under complex mixing and low-load conditions. Seven macroscopic optical properties are used to construct a set of constraint equations, and least-squares inversion with Monte Carlo sampling is applied to decompose the 532 nm backscatter coefficient into contributions from smoke, urban aerosols, pollen, and dust. This framework extends the approach of Veselovskii et al. (2024) by enhancing parameter dimensionality and stability. Section 2 details the methodology, and Section 3 presents validation, sensitivity analysis, and case studies.

2 Data and method

2.1 Lidar equipment

Situated at the summit of Damaojian Mountain (119.50° E, 28.58° N, 1128 m) in Wuyi, Zhejiang, the Atmospheric Boundary Layer Eco-Environment Shanghuang Observatory (ABLES) serves as a key meteorological station at the top of the boundary layer, surrounded by rich forest resources (Wang et al., 2025). The site operates an advanced multiwavelength lidar system integrated with Mie, Raman, and fluorescence channels. This system detects backscatter signals across six wavelength bands: three elastic channels at 355, 532, and 1064 nm, with the 355 and 532 nm channels equipped for depolarization measurements via vertical and horizontal components; two Raman channels at 386 and 607 nm corresponding to excitation wavelengths of 355 and 532 nm, respectively; and a single fluorescence channel at 466 nm induced by the 355 nm emission. (Fig. S1a). Data collection is performed with a temporal resolution of 15 minutes and a vertical resolution of 15 m. Due to the blind zone of the lidar, valid data are available starting from a minimum height of 190 m. Detailed technical specifications of the lidar system

https://doi.org/10.5194/egusphere-2026-2017
Preprint. Discussion started: 29 April 2026

are summarized in Table 1. It is important to note that all vertical coordinates and height information presented in this study refer to the height above the mountain summit (above ground level), rather than the altitude above mean sea level.

Table 1: Main Parameters of the Lidar System.

Definition	Reference value
Operating wavelengths	355 nm / 532 nm / 1064 nm
Maximum pulse repetition frequency	10 Hz
Pulse width	< 10 ns
Lamp lifetime	50,000,000 pulses
Measurement distance	10 km
Telescope type	Cassegrain
Primary mirror diameter	≥ 300 mm
Focal length	940 mm
Field of view	1 mrad
Number of detection / receive channels	8
Filter bandwidth (peak / FWHM)	≤ 1 nm
Filter bandwidth (fluorescence)	44 nm
Photon-counting sampling rate	> 20 MHz
Spatial resolution	15 m

Photon counting signals acquired by the lidar system first undergo preprocessing, including background subtraction, overlap correction, and range-square correction. Preliminary retrievals are subsequently conducted based on these pre-processed data (Fig. S1b). For the elastic (Mie) channels, aerosol optical parameters are retrieved using the Fernald algorithm (Fernald, 1984), which separates total extinction and backscattering into molecular and aerosol contributions. The aerosol extinction coefficient profile is obtained by assuming an aerosol lidar ratio and applying boundary conditions at a reference height. Following the retrieval of aerosol extinction coefficients at the laser wavelengths, the Ångström power law is applied to extrapolate these coefficients to the wavelengths of the fluorescence and Raman channels for the calculation of path transmittance. Based on this transmittance correction, the fluorescence backscatter coefficient (β_F) is subsequently retrieved from the fluorescence and Raman signals. This methodology has been systematically applied and validated in recent research involving multichannel fluorescence and Raman lidar observations and algorithm development (Veselovskii et al., 2020; Gast et al., 2025; Huang et al., 2025). In parallel, for the Raman channels, the aerosol extinction coefficient is retrieved independently by exploiting the combined attenuation relationship of the Raman scattering echo at both the laser and Raman wavelengths. This approach circumvents the need for aerosol lidar ratio assumptions, which reduces dependency on priors and minimizes systematic errors (Ortiz-Amezcua et al., 2020; Zhao et al., 2021). Data from the Raman and fluorescence channels exhibit high reliability at night owing to robust signal-to-noise ratios but are sensitive to background light during daytime. Therefore, this study exclusively utilizes observations from April to December 2023, restricted to the hours of 18:00 LST to 07:00 LST the following day, to guarantee data reliability.

https://doi.org/10.5194/egusphere-2026-2017
Preprint. Discussion started: 29 April 2026

2.2 Aerosol classification and quantitative retrieval algorithm

To exploit the observational capabilities of multiwavelength Raman–fluorescence lidar for the precise classification and quantitative retrieval of vertical aerosol distributions, we developed a multiparameter constrained algorithm based on the principle of least squares. This algorithm models complex atmospheric aerosol layers as external mixtures composed of four predefined fundamental types: smoke, urban, pollen, and dust. The contribution of each type to the particle backscatter coefficient at 532 nm derived from the Raman channel (β_R) is denoted by η_i (defined as the ratio of β_i and β_R, where i represents the aerosol type). The core hypothesis of the algorithm posits that the macroscopic optical properties of the mixed aerosol are a linear weighted combination of the optical properties of each pure type, where the weighting coefficients directly correspond to η_i, which satisfy a normalization constraint with their sum equal to unity:

$$\sum_{i\in\{s,p,u,d\}} \eta_i = 1, \tag{1}$$

The model integrates multidimensional optical parameters as joint constraints to accurately distinguish aerosol types within complex mixtures. Initially, fluorescence capacity G_F serves as a key constraint, leveraging the distinct fluorescence signatures of bioaerosols. Its definition and the corresponding linear mixing rule are expressed as:

$$G_F = \frac{\beta_F}{\beta_R} \tag{2}$$

$$G_F = \sum_{i\in\{s,p,u,d\}} \eta_i G_F^i \tag{3}$$

The introduction of G_F significantly enhances the capability of the model to identify biogenic types, which addresses the limitations of traditional aerosol lidar systems. Second, regarding the particle depolarization ratio (*PDR*), a vital parameter describing particle nonsphericity, direct linear mixing would introduce systematic errors because this parameter does not physically satisfy a linear superposition law. Therefore, the linear depolarization ratio *PDR'* is utilized for calculation. The calculation formula and mixing rule are expressed as:

$$PDR'_\lambda = \frac{PDR_\lambda}{1+PDR_\lambda} \tag{4}$$

$$PDR'_{\lambda,obs} = \sum_{i\in\{s,p,u,d\}} \eta_i PDR'^i_{\lambda,obs} \tag{5}$$

Furthermore, to fully utilize the multiband detection capabilities of the lidar, the model incorporates constraints on spectral dependence and backscattering efficiency. By introducing *BÅE*, the relationship of backscatter intensity between different wavelengths is transformed into a Color Ratio (*Cr*) constraint:

$$Cr^{obs}_{\lambda_1/\lambda_2} = \sum_{i\in\{s,p,u,d\}} \eta_i \left(\frac{\lambda_2}{\lambda_1}\right)^{AE^i_{\lambda_1,\lambda_2}} \tag{6}$$

Simultaneously, the *LR* constraints are formulated as:

$$LR^{obs}_\lambda = \sum_{i\in\{s,p,u,d\}} \eta_i LR^i_\lambda \tag{7}$$

https://doi.org/10.5194/egusphere-2026-2017
Preprint. Discussion started: 29 April 2026

In summary, leveraging the availability of multiple macroscopic optical variables at multiple wavelengths, the model constructs a system of least-squares equations defined by Eqs. 3–7. The application of these equations yields a set of seven macroscopic optical constraints G_F, PDR_{355}, PDR_{532}, $Cr_{355/532}$, $Cr_{1064/532}$, LR_{355}, and LR_{532}. Regarding the retrieval strategy, acknowledging that the optical properties of pure aerosol types in nature are not fixed constants but fluctuate within a certain range due to factors such as aging, transport pathways, and ambient humidity, the algorithm employs Monte Carlo simulations to address this parameter uncertainty. For each spatiotemporal pixel at every vertical height, the model executes N=100 independent random trials. In each trial, the macroscopic optical parameters of each pure aerosol type are randomly resampled from a uniform distribution. These ranges are statistically determined based on a comprehensive review of lidar research from various Eurasian teams over the last decade (2015–2025) regarding the optical properties of Smoke, Urban, Pollen, and Dust types (Table S1), as visually represented in Figure 1a-d.

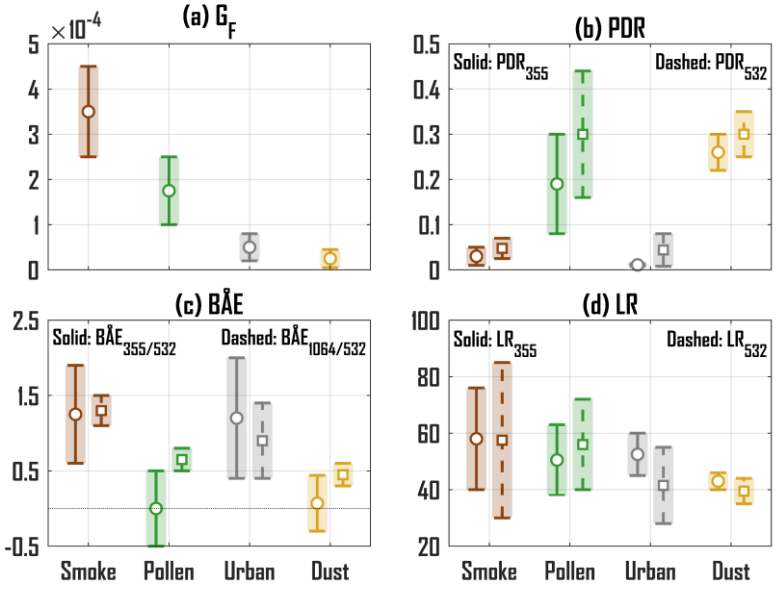

Figure 1: Reference ranges of seven macroscopic optical parameters for the four pure aerosol types.

The primary objective of solving this linear system is to determine the optimal vector of aerosol type fractions that minimizes the deviation between the model-predicted optical parameters $y_k^{mod}(\eta)$ and the observed values y_k^{obs}, with k referring to each constraint variable. This deviation is quantified by the cost function χ^2, defined as the sum of squared weighted residuals:

$$\chi^2(\eta) = \sum_k \left(\frac{y_k^{mod}(\eta) - y_k^{obs}}{\sigma_k} \right)^2 \quad (8)$$

In Eq. 8, the weighting factor σ_k is dynamically defined as the maximum of the standard deviation of the pure aerosol type samples in the current Monte Carlo trial and a 5% relative observation error. This weighting strategy balances the influence of parameters with distinct physical magnitudes. To ensure the physical plausibility of the retrieval, a non-negativity constraint

https://doi.org/10.5194/egusphere-2026-2017
Preprint. Discussion started: 29 April 2026

is strictly enforced during the solution process ($\eta_i \geq 0$). Finally, the reported fractional contributions for the four aerosol types are derived as the statistical mean of the solutions from all Monte Carlo trials. Following the determination of η_i, the mass concentration for each aerosol type (C^i_{mass}) is calculated via:

$$C^i_{mass} = \eta_i \cdot \beta_{532} \cdot LR^i_{532} \cdot C^i_V \cdot \rho^i \quad (9)$$

Here, LR^i_{532} represents the lidar ratio of each aerosol type at 532 nm. C^i_V denotes the extinction-to-volume conversion coefficient used to convert the extinction coefficient into volume concentration, which is subsequently converted to mass concentration via the density ρ^i. The relevant parameters are listed in Table 2 (Veselovskii et al., 2024; Filioglou et al., 2025). Since data below 190 m is considered invalid due to the blind zone, linear interpolation is utilized to fill the data gap in the 50 m to 190 m height range.

Table 2: Lidar ratios, extinction-to-volume conversion coefficients, and density values for the four pure aerosol types

Type	LR_{532}	C_V (μm^3 cm^{-3} Mm)	ρ (g cm^{-3})
Smoke	64	0.13	1.15
Urban	61	0.35	1.50
Pollen	60	1.79	0.80
Dust	45	0.70	2.60

2.3 Auxiliary datasets

2.3.1 CALIPSO satellite data

This study utilized the Cloud-Aerosol Lidar and Infrared Pathfinder Satellite Observations (CALIPSO) Lidar Level 2 Aerosol Profile, Version 4-51 data product (https://asdc.larc.nasa.gov/project/CALIPSO/CAL_LID_L2_05kmAPro-Standard-V4-51_V4-51, last access: 7 November 2025), provided by the Atmospheric Science Data Center (ASDC) (Nasa/Larc/Sd/Asdc). This dataset covers observational records in 2023 and provides the vertical distribution of aerosol optical parameters with a horizontal resolution of 5 km. Specifically, we employed the 532 nm Total Backscatter Coefficient profiles from this product as a spaceborne reference benchmark. These profiles served to validate and evaluate the backscatter coefficient retrievals derived from the Mie and Raman channels of the ground-based lidar, as detailed in Section 3.1.1.

2.3.2 Ground-based and airborne validation data

To validate the classification algorithm across multiple dimensions, we acquired station monitoring data from ABLES. These observational records include $PM_{2.5}$ and PM_{10} mass concentration data with a temporal resolution of 1 minute, covering the period from April 1 to December 31, 2023, which facilitated ground-level validation of aerosol mass concentration. Furthermore, to assess the performance of the lidar fluorescence channel in the vertical, we conducted a targeted unmanned aerial vehicle (UAV) observation experiment at ABLES on December 11, 2025 (Fig. 3a-c). The experimental platform utilized

https://doi.org/10.5194/egusphere-2026-2017
Preprint. Discussion started: 29 April 2026

a DJI M400 UAV equipped with a ZR-7500 bioaerosol monitor. These observations covered a height range from ground level to 500 m, yielding vertical profiles of bioaerosol number concentration at four specific times (11:57, 12:45, 14:00, and 15:24 LST), as detailed in Section 3.1.1.

2.3.3 Meteorological reanalysis data

This study incorporated ERA5 reanalysis data provided by the European Centre for Medium-Range Weather Forecasts (ECMWF) to analyze the influence of meteorological conditions on aerosol distribution. We selected hourly pressure-level data for the year 2023, characterized by a spatial resolution of 0.25° × 0.25° and a temporal resolution of 1 hour. The extracted variables include temperature (T), relative humidity (RH), horizontal wind components (U, V), and vertical velocity (W). Spatial interpolation was applied to map the data to the study location. All data were accessed via the Copernicus Climate Data Store (https://cds.climate.copernicus.eu/datasets/, last access: 7 October 2025).

3 Results and discussion

3.1 Validation of retrieval results

3.1.1 Vertical validation of the Mie–Raman–fluorescence channels

To validate the retrieval accuracy of the ground-based lidar Mie and Raman channels at 532 nm, this study employed the CALIPSO Level 2 Standard Aerosol Profile Product for cross-comparison. Given the polar orbit trajectory of the spaceborne CALIPSO lidar, we selected observational data that were spatially closest to the ABLES site (linear distance of 12.6 km) and temporally synchronized. As illustrated in Figure 2a, the CALIPSO-retrieved backscatter coefficient at 532 nm (β_{532}) indicates that aerosol layers with strong scattering are mainly confined to the near-surface region below 0.5 km (marked by the triangle), while β_{532} decreases markedly above 0.5 km, consistent with clean atmospheric conditions. Considering that the ABLES is situated at an altitude of 1128 m, this elevation resides above the near-surface aerosol layer observed by the satellite. A comparison with the simultaneous ground-based lidar observations (marked by the star in Figure 2b) reveals that β_{532} retrieved by both the Mie and Raman channels at the lidar starting height (above 1128 m) remain at an extremely low level (approximately 10^{-4} $km^{-1}sr^{-1}$), maintaining a high degree of consistency in magnitude with the clean background values observed by CALIPSO at the same height.

Furthermore, regarding the dynamic range of the numerical distribution, the two datasets exhibit a high degree of agreement. Both in high-scattering aerosol regions and low-scattering background zones, the ground-based lidar retrievals fall within a similar physical magnitude range to the CALIPSO product (10^{-4} to 10^{-2} $km^{-1}sr^{-1}$). This observed consistency suggests that the Mie-Raman retrieval algorithm can reliably capture fluctuations in aerosol concentration and maintains quantitative stability across the linear response interval ranging from strong to weak signals.

https://doi.org/10.5194/egusphere-2026-2017
Preprint. Discussion started: 29 April 2026

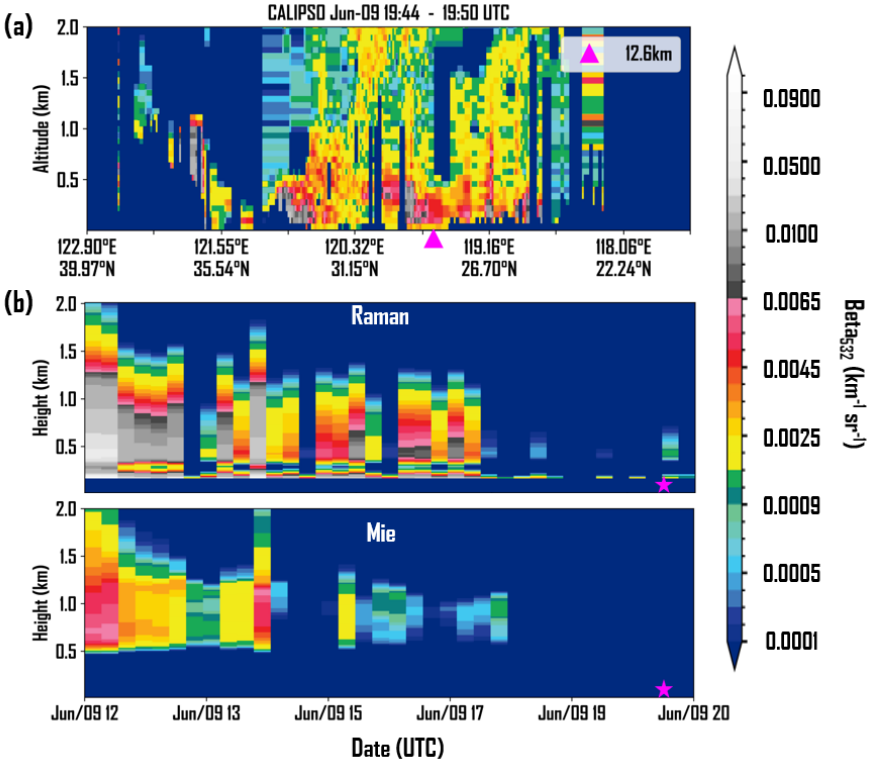

Figure 2: Comparison of β_{532} profiles. (a) Retrieval product from the CALIPSO Level 2 standard data. (b) Retrievals from the Mie and Raman channels of the ground-based multiwavelength lidar.

The validation of the fluorescence channel was conducted by assessing the vertical distribution of bioaerosol number concentration $N_{\mathrm{bio}}(z)$, which is derived from β_{F} using Eq.10:

$$N_{bio}(z) = \frac{\beta_F}{\sigma_{bio}^F \cdot \Delta\lambda} \tag{10}$$

Here, $\sigma_{\mathrm{bio}}^{\mathrm{F}}$ represents the fluorescence cross-section, adopted as 10^{-11} cm^2 sr^{-1} nm^{-1} (Rao et al., 2018), and $\Delta\lambda$ denotes the bandwidth of the fluorescence channel filter (44 nm). For vertical validation, lidar results were compared with UAV-based instrument observations. Since the fluorescence signal is restricted to nighttime operation, the combination of nighttime lidar data and daytime instrument data characterizes the diurnal temporal evolution of bioaerosols, as illustrated in Figure 3d. The airborne measurements, continuous along the vertical, are seamlessly integrated with the lidar observations, which are continuous in both time and altitude. High bioaerosol concentrations were observed between 400 and 500 m from early morning to noon. By 15:24 LST, however, and in subsequent evening lidar profiles, the concentration peak had descended to below 350 m, reflecting the diurnal variation of the mixing layer height. These observations validate the effectiveness of the macroscopic optical variables retrieved from the lidar fluorescence channel.

https://doi.org/10.5194/egusphere-2026-2017
Preprint. Discussion started: 29 April 2026

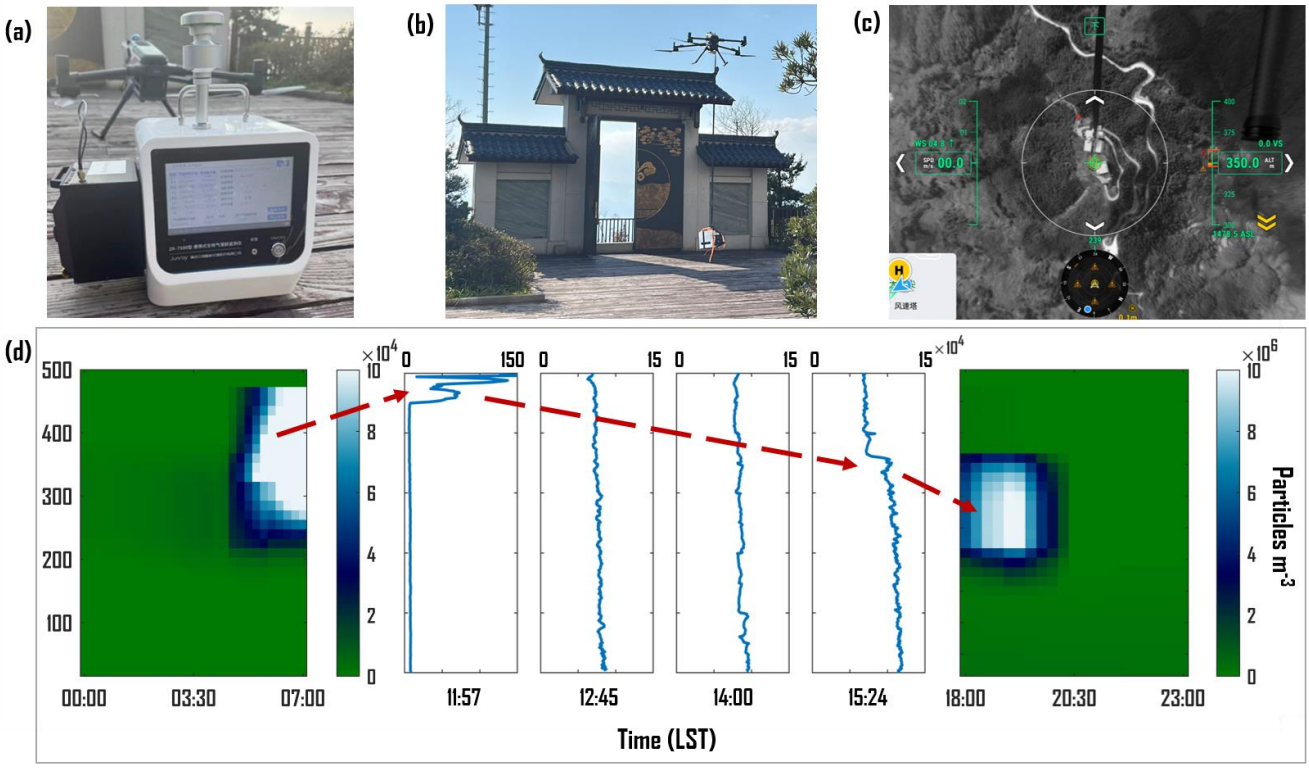

Figure 3: UAV-based validation experiment and diurnal bioaerosol profiling. (a) ZR-7500 bioaerosol instrument. (b) On-site photograph of the UAV operation at ABLES. (c) Aerial image from the flight. (d) Vertical profiles of bioaerosol number concentration on 11 December 2025, showing the temporal connection between daytime UAV data and nighttime lidar retrievals.

3.1.2 Ground-level validation of particulate matter

Figure 4a-b show a comparison between the $PM_{2.5}$ and PM_{10} mass concentrations retrieved by the lidar and the corresponding in situ measurements at ABLES. The retrieved $PM_{2.5}$ (sum of Smoke and Urban types) and PM_{10} (sum of Pollen and Dust types) both show favorable agreement with ground observations, characterized by coefficients of determination (R^2) exceeding 0.6 and root mean square errors (RMSE) below 14.2 μg m^{-3}. This suggests a reasonable level of quantitative consistency at the ground scale.

Regarding seasonal characteristics, the retrieval performance exhibits significant seasonal variability. While winter retrievals achieve the highest accuracy due to low aerosol loading ($PM_{2.5}$ < 25 μg m^{-3}; PM_{10} < 60 μg m^{-3}) and tight clustering along the 1:1 line, autumn exhibits elevated $PM_{2.5}$ levels (>80 μg m^{-3}) driven by transport or accumulation effects. The algorithm nonetheless maintains robust performance under these conditions. Conversely, spring data display the most significant scatter, likely due to complex aerosol mixing involving dust and pollen. Similarly, the dispersion and partial overestimation observed between the retrieved sum of pollen and dust and in-situ PM_{10} measurements are reasonable. This is attributed to the presence of intact pollen grains, which often have diameters larger than 10 μm. These giant particles contribute to the optical retrieval yet are filtered out by the sampling inlets of ground-based PM_{10} instruments, leading to the observed deviation.

https://doi.org/10.5194/egusphere-2026-2017
Preprint. Discussion started: 29 April 2026

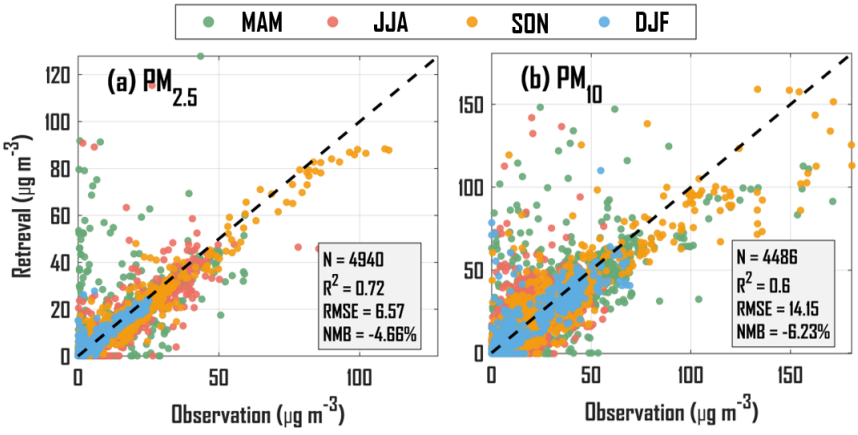

Figure 4: Comparison of in situ observations with the bottom-layer retrieved mass concentrations at ABLES for (a) $PM_{2.5}$ and (b) PM_{10}.

3.2 Classification results

3.2.1 Vertical profiles of aerosol mass concentrations

Vertical mass concentration profiles for four aerosol types (smoke, urban, pollen, and dust) were retrieved using seven physical constraints: G_F, PDR_{355}, PDR_{532}, $Cr_{355/532}$, $Cr_{1064/532}$, LR_{355}, and LR_{532}. (Figure 5a). For comparison, Figure 5b presents retrieval results constrained only by G_F and PDR_{532}. Although G_F (the ratio of β_F to β_R) is a critical parameter for aerosol typing, it is highly sensitive to RH and cannot be used for direct classification or quantification without humidity correction (Veselovskii et al., 2024). RH influences G_F through two distinct pathways by increasing β_R due to hygroscopic growth (associated with changes in particle volume or refractive index) while simultaneously decreasing β_F via fluorescence quenching, dilution, or phase changes. The combined effect of these processes significantly alters the magnitude of G_F, leading to bias or increased uncertainty in classification schemes primarily based on this parameter (Veselovskii et al., 2025). Consequently, incorporating additional physical constraints is essential to improve algorithm. Compared with the dual-parameter approach, the multi-constraint retrieval enables clearer aerosol differentiation. Notably, urban aerosol concentrations are significantly lower compared to the dual-parameter results, while near-surface pollen features are more pronounced. This distribution is consistent with the ecological context of the ABLES, which is characterized by abundant forest resources and low anthropogenic pollution levels.

https://doi.org/10.5194/egusphere-2026-2017
Preprint. Discussion started: 29 April 2026

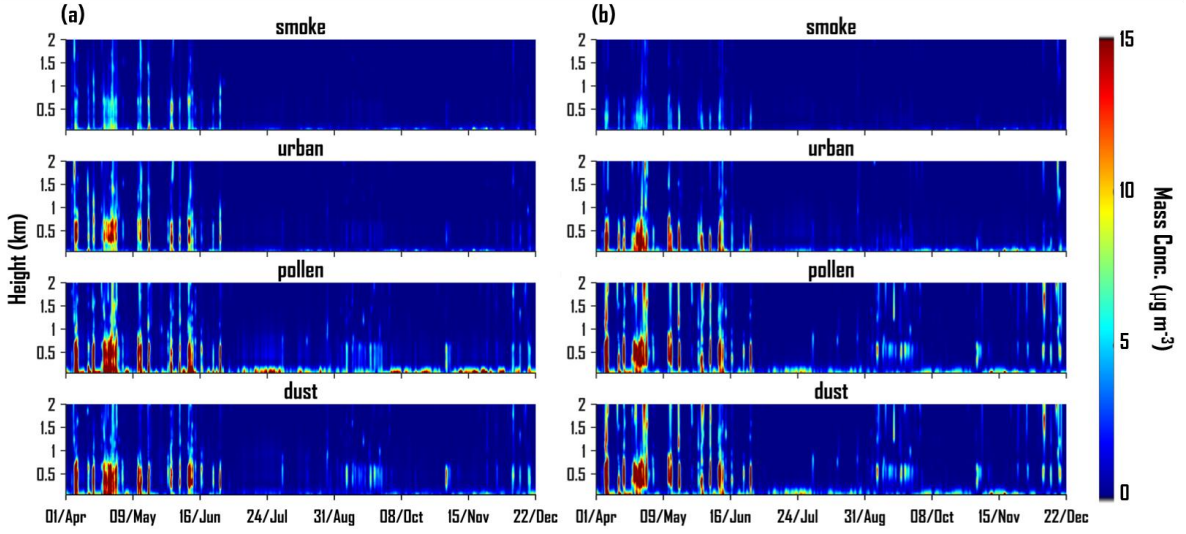

Figure 5: Vertical profiles of mass concentrations for four aerosol types (smoke, urban, pollen, and dust) in 2023. (a) Retrieval results based on seven physical constraints. (b) Retrieval results based on dual constraints (G_F and PDR_{355}). The unit is μg m^{-3}.

3.2.2 Sensitivity analysis

Among the multi-dimensional macroscopic optical parameters of the four aerosol types (smoke, urban, pollen, and dust), G_F exhibits exceptional discriminatory performance. Due to the distinct, non-overlapping distributions of its characteristic values (Figure 1), the algorithm demonstrates high robustness to perturbations in G_F, rendering its contribution to relative classification bias negligible. Consequently, this sensitivity analysis focuses on the response of retrieved scattering contributions at 532 nm to the other macroscopic optical parameters, including *PDR*, *BÅE*, and *LR*, where optical signatures exhibit varying degrees of overlap. These parameters serve as indicators of particle non-sphericity, size distribution, and optical behavior. We introduced a 20% perturbation to the reference ranges of the seven macroscopic optical variables for each aerosol type to evaluate the resulting relative deviations in the output scattering contributions, with a primary focus on how sensitivity varies across vertical heights and seasons.

The sensitivity of the retrieved backscatter contributions from different aerosol types to *PDR* perturbations shows pronounced seasonal and vertical variability (Figure 6). In spring, pollen aerosols in the near-surface layer at the mountain summit (0.15–0.30 km) exhibit an exceptionally strong response to perturbations in the 355 nm *PDR* (PDR_{355}) (Figure 6a). This layer is characterized by high local pollen concentrations driven by gravitational settling. Despite the relatively low PDR_{355} of pollen (Bohlmann et al., 2021), the intense molecular Rayleigh scattering at this wavelength increases measurement noise, which propagates into the retrieved aerosol signal and degrades the effective signal-to-noise ratio, even after background correction. Under these conditions, coarse-mode particles situated in the geometric optics regime serve as a strong constraint for interpreting fluctuations in non-spherical signals.

https://doi.org/10.5194/egusphere-2026-2017
Preprint. Discussion started: 29 April 2026

The retrieval sensitivity of urban aerosols to perturbations in PDR_{532} peaks in the 0.15–0.30 km layer during spring (Figure 6b). In this season, the atmosphere surrounding the high-altitude site is frequently influenced by the regional transport of anthropogenic pollution coupled with dust deposition, forming a complex "haze-dust" external mixture. Consequently, aerosols exhibit a variable mixing state characterized by highly sensitive optical properties (Reddy et al., 2019; Li et al., 2023). This results in significantly elevated 532 nm particle depolarization ratios within 300 m above the mountain top, accompanied by substantial spatiotemporal variability. In summer, the sensitivity zone shifts upward to 0.3–0.8 km. This shift corresponds to the uplift of the local mountain planetary boundary layer driven by intense solar radiation, allowing the mixing layer height to extend from several hundred meters to approximately 1 km above the summit in the afternoon (Solanki et al., 2021; Singh et al., 2016). During this period, aerosols lifted to the upper mixing layer by valley breezes and thermal circulation are exposed to high temperature, high humidity, and strong turbulence. These conditions promote significant hygroscopic growth and an evolution toward spherical morphology. As a result, this layer falls precisely within the optical transition zone between spherical and non-spherical particles, where the depolarization ratio exhibits large vertical fluctuations and seasonal differences in response to minute variations in composition and morphology (Chiang et al., 2023). In winter, the sensitivity of urban aerosols to PDR_{532} appears primarily within the height range of 0.8–1.2 km. This layer is dominated by long-range transported aged smoke or residual aerosols. Having undergone prolonged heterogeneous chemical reactions and cloud processing (Fu et al., 2020), their microphysical characteristics deviate significantly from the assumptions of standard urban aerosol models, resulting in high uncertainty in the retrieval of such particles.

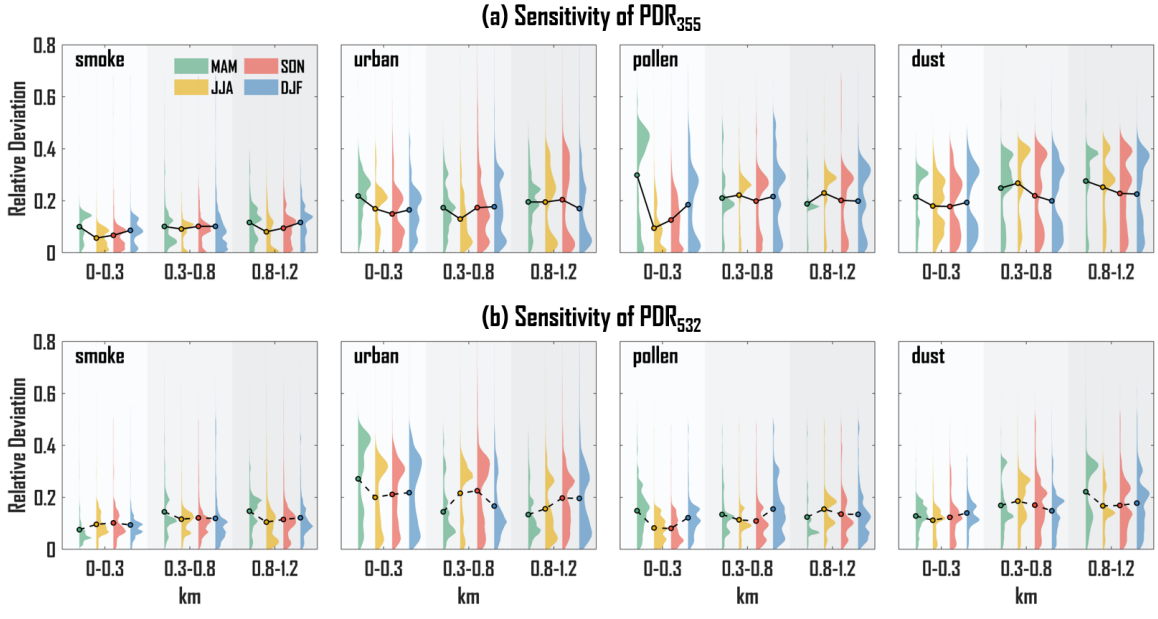

Figure 6: Sensitivity of the scattering contribution fractions (the ratio of β_i and β_R) of four aerosol types to perturbations in (a) PDR_{355} and (b) PDR_{532}.

https://doi.org/10.5194/egusphere-2026-2017
Preprint. Discussion started: 29 April 2026

Perturbation sensitivity analysis of *BÅE* elucidates the intrinsic link between the seasonal evolution of aerosol microphysical size and spectral wavelength dependence (Figure 7a-b). Smoke aerosols exhibit the lowest sensitivity to *BÅE* perturbations within the height range of 0.8–1.2 km. This stability arises from the prevalence of long-range transported smoke plumes captured at the high-altitude station during the active Northern Hemisphere biomass burning season. Driven by coagulation and organic condensation during transport, the particle size distribution of these plumes converges from the Aitken mode into a singular, highly uniform accumulation mode, with an effective radius stabilizing at approximately 0.2–0.3 μm (Mylonaki et al., 2021). Such size homogeneity imparts aged smoke with a distinct and stable *BÅE* spectral fingerprint, acting as a strong constraint within the retrieval space.

Urban aerosols display pronounced sensitivity within the 0.3–0.8 km layer during summer and autumn. During these seasons, intense solar radiation drives the vigorous vertical development of the local mountain convective boundary layer (CBL), which frequently extends to heights exceeding 0.8 km (Solanki et al., 2021). Coupled with the high-humidity environment characteristic of the monsoon, these conditions trigger drastic hygroscopic growth in hydrophilic aerosols, causing the *BÅE* to decline sharply and non-linearly with increasing humidity (Cheng et al., 2025). Within this high-gradient regime, even minute *BÅE* perturbations are amplified by the algorithm and interpreted as shifts in hygroscopic state or mode mixing, thereby increasing retrieval uncertainty.

Pollen aerosols exhibit significantly higher sensitivity to perturbations in $BÅE_{355/532}$ than in $BÅE_{532/1064}$. Fundamentally, this stems from the fact that pollen diameters far exceed visible and near-infrared wavelengths. Consequently, in the 532–1064 nm band, pollen falls within the geometric optics regime where the scattering efficiency factor converges to a constant of 2, rendering $BÅE_{532/1064}$ physically flat. In contrast, at the shorter ultraviolet wavelength (355 nm), radiation continues to interact with non-spherical surface microstructures and specific fluorescent constituents, allowing $BÅE_{355/532}$ to retain sensitivity to spectral slope variations. The sensitivity peak observed at 0.8–1.2 km coincides with the transition zone at the top of the summer mountain CBL. In this region, enhanced wind shear and static stability drive intense horizontal and vertical stratification, alongside transitions in the mixing state between pollen clusters and background fine particles. Furthermore, high humidity induces weak hygroscopic swelling of the coarse, hydrophilic pollen exine and attached fine particulates—an effect that is optically amplified at 355 nm. As a result, pollen sensitivity maximizes within this layer, particularly during summer.

For dust aerosols, the sensitivity to perturbations in *BÅE* peaks within the near-surface layer (0.15–0.3 km), exhibiting a distinct seasonal pattern where summer and autumn intensities exceed those of spring and winter. During the spring outbreak season, the dominance of high-concentration, pure dust particles establishes a robust classification boundary within the BAE parameter space, ensuring high retrieval certainty. In contrast, during summer and autumn, effective wet scavenging processes reduce dust to a low-abundance background mode or a hygroscopic mixed state (Zhang et al., 2025). Consequently, this transition to a physically complex, diluted state renders the retrieval algorithm significantly more sensitive to BAE perturbations in the near-surface layer during these warmer seasons.

https://doi.org/10.5194/egusphere-2026-2017
Preprint. Discussion started: 29 April 2026

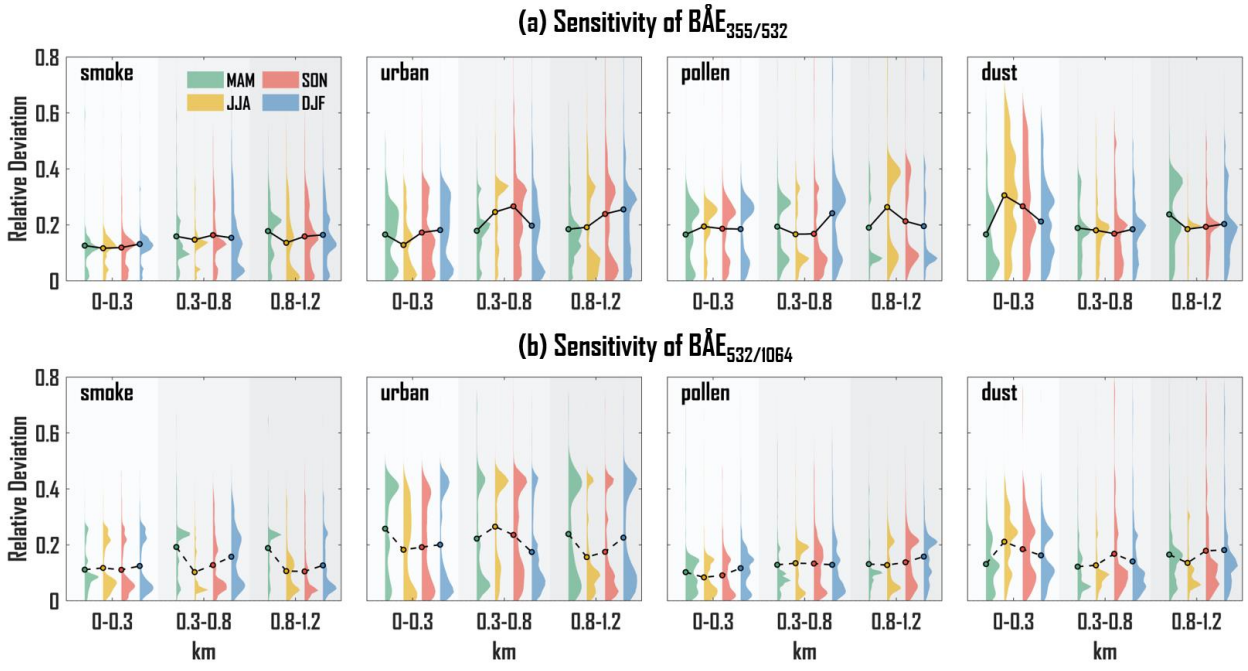

Figure 7: Sensitivity of the scattering contribution fractions (the ratio of β_i and β_R) of four aerosol types to perturbations in (a) $BÅE_{355/532}$ and (b) $BÅE_{532/1064}$.

Sensitivity analysis of the lidar ratio (LR) elucidates the seasonal coupling mechanisms linking the spectral dependence of the imaginary refractive index, hygroscopicity-induced optical phase transitions, and vertical boundary layer dynamics (Figure 8a-b). In the near-surface layer (0-0.3km), both urban and dust aerosols share a consistent spectral divergence pattern characterized by sensitivity to LR_{355} in spring and winter versus LR_{532} in summer and autumn. This phenomenon is governed by a seasonal regime shift between absorption-dominated and scattering-dominated mechanisms. During cold seasons (winter or spring), anthropogenic heating emissions and thermal inversions facilitate the accumulation of Black Carbon (BC) and mineral dust. These components exhibit a strong imaginary refractive index response at 355 nm, where minute *LR* perturbations generate significant uncertainty via non-linear amplification of the absorption term. Conversely, the summer and autumn months are characterized by reduced absorbing constituents and intense hygroscopic growth driven by high humidity (Li et al., 2025). This shifts the size parameter of urban aerosols into the 532 nm Mie scattering resonance regime, where the scattering phase function becomes highly sensitive to minute fluctuations in particle water content. Vertically, the diminishing sensitivity of urban aerosols to LR_{355} with altitude reflects aging and coating effects. As BC cores become encapsulated by non-absorbing secondary salts during vertical diffusion, their UV absorption efficiency decreases, thereby reducing the weight of LR355 in the retrieval equation. For pollen aerosols, characterized by large particle size and non-sphericity, the retrieval sensitivity to LR_{355} and LR_{532} is inherently governed by the vertical distribution of the aerosol load. Specifically, peak sensitivity is confined to the near-source layer (below 0.8 km) in spring and winter due to stable stratification, whereas strong convective uplift and transport during summer and autumn shift the layer of maximum sensitivity to higher altitudes (0.8–1.2 km).

https://doi.org/10.5194/egusphere-2026-2017
Preprint. Discussion started: 29 April 2026

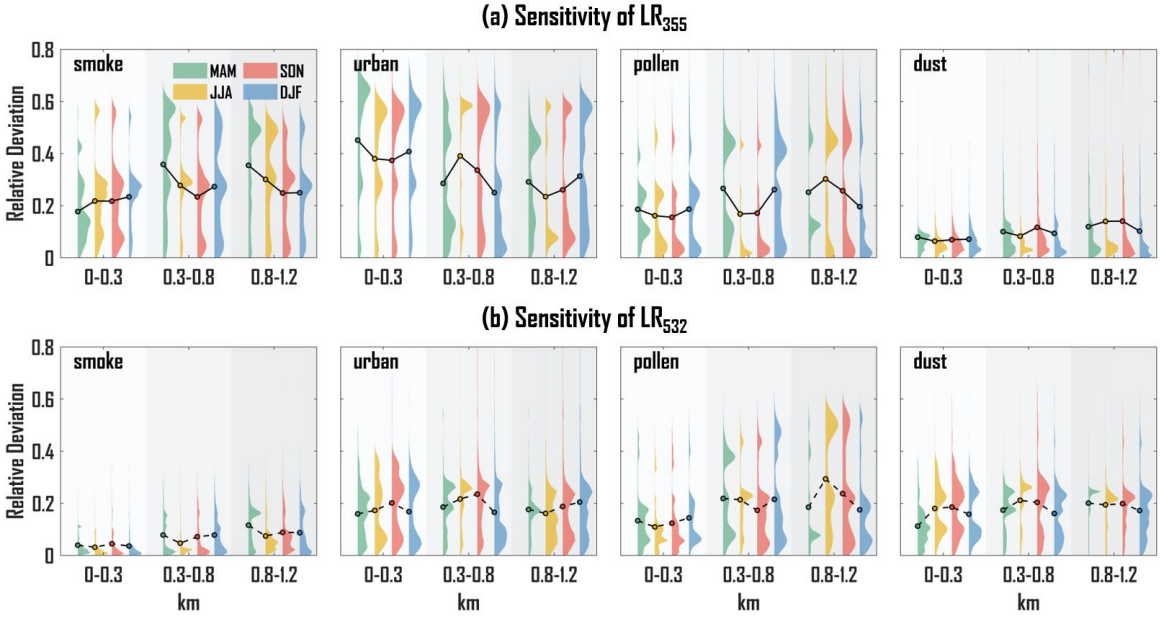

Figure 8: Sensitivity of the scattering contribution fractions (the ratio of β_i and β_R) of four aerosol types to perturbations in (a) LR_{355} and (b) LR_{532}.

3.3 Case studies

Between April 11 and 12, 2023, lidar observations revealed a significant surge in β_{532} below 1 km (Figure 9a), coinciding with a synchronous increase in the mass concentrations of multiple aerosol types. Retrieval results indicate that urban aerosol mass concentrations exceeded 15 μg m^{-3}, while both pollen and dust concentrations surpassed 60 μg m^{-3} (Figure 9c). In terms of vertical evolution, a distinct "wedge-shaped" subsidence pattern emerged from April 10 to 11. Over time, the layer dominated by dust scattering (contribution fraction > 0.5) descended from 1.2 km to below 0.5 km (Figure 9b). Concurrently, the pollen layer closely tracked the upper boundary of the dust layer, and together they constituted the primary scattering strata.

Analysis of scattering contributions alongside wind field correlations suggests this high-concentration episode resulted from the coupling of regional transport and local meteorological conditions. Notably, urban and dust aerosols exhibited high vertical consistency. Within the 0.5–1 km range, their distribution showed a significant positive correlation (R up to 0.91) with both horizontal (u, v) and vertical (w) wind speeds (Figure 10a-d). This spatiotemporal coherence implies physicochemical interactions beyond simple co-transport. In mixed plumes, anthropogenic inorganic precursors undergo heterogeneous reactions or thermodynamic partitioning on mineral dust surfaces to form soluble coatings, such as nitrate. This aging process enhances dust hygroscopicity and facilitates the coagulation of fine-mode urban aerosols onto coarse-mode dust (Milousis et al., 2025). Consequently, the observed correlation and synchronous settling reflect chemical aging and microphysical coagulation within the urban–dust mixture, while strong winds drive the advection of these processed upstream air masses.

https://doi.org/10.5194/egusphere-2026-2017
Preprint. Discussion started: 29 April 2026

Meteorological reanalysis links the formation of these high values to stable atmospheric stratification. From 00:00 to 08:00 LST on April 11, a distinct temperature inversion occurred at approximately 0.5–1 km (Figure 10e), indicating significantly enhanced atmospheric static stability that effectively suppressed vertical turbulent exchange.This stratification restricted the vertical redistribution of aerosols, causing optical structures to stagnate and intensify within this layer. Additionally, relative humidity remained at moderate levels (50%–70%, Figure 10f). Although sufficient to initiate uptake on aged particles, this range is generally below the threshold for the dominant hygroscopic growth observed in pure salts or droplets (Wise et al., 2007). Therefore, the observed enhancement in scattering contribution is likely primarily driven by changes in particle size distribution and scattering phase function, particularly an increased fraction of optically efficient particles, rather than to a net increase in aerosol mass. This indicates a decoupling between optical response and mass concentration driven by microphysical aging processes under stable stratification.

Fig. S2 illustrates the temporal evolution of meteorological variables from April 9 to April 12, 2023. The explosive growth in urban, pollen, and dust mass concentrations during the early morning of April 12 (00:00–08:00) was primarily driven by relative humidity exceeding 80%. This high-humidity environment led to the formation of cloud layers, as evidenced by the backscatter coefficient β_R exceeding 1 km^{-1} sr^{-1}. During this period, mass concentrations for all aerosol types surged, with pollen and dust exceeding 50 μg m^{-3}. This pollution episode was driven by two coupled processes: hygroscopic growth and cloud processing, which enhanced single-particle scattering efficiency, and the evolution of the nocturnal boundary layer, which trapped pollutants within residual or stable layers. Furthermore, weak horizontal and vertical winds below 1 km facilitated the local accumulation of pollutants.

In contrast, Fig. S3 shows that smoke aerosols dominate the β_R from October 15 to 18, 2023. Since the extinction-to-volume conversion factor (C_V) for smoke is one order of magnitude lower than that for pollen, the mass concentration of smoke remains low even though it contributes significantly to the extinction coefficient. This indicates that the algorithm can effectively identify the optical contributions of different aerosol types under low aerosol loading conditions.

https://doi.org/10.5194/egusphere-2026-2017
Preprint. Discussion started: 29 April 2026

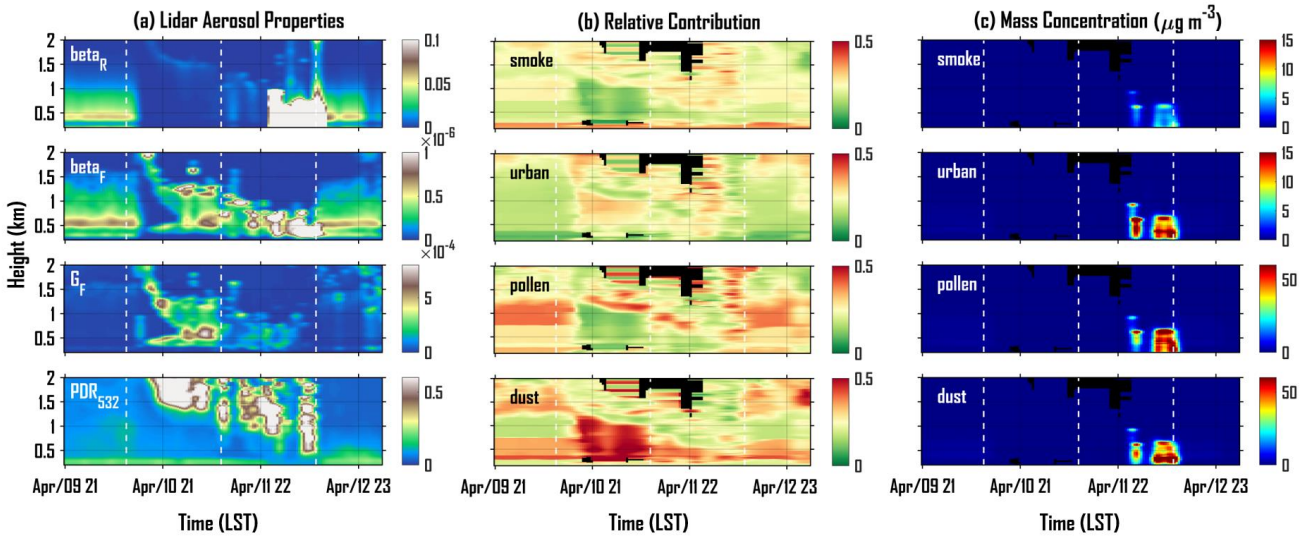

Figure 9: Vertical profiles from April 9 to 12, 2023: (a) 532 nm backscatter coefficient (β_R, km^{-1} sr^{-1}), fluorescence backscatter coefficient (β_F, km^{-1} sr^{-1}), fluorescence capacity, and 532 nm depolarization ratio (PDR_{532}); (b) relative contributions of smoke, urban, pollen, and dust to (β_R); and (c) mass concentrations of the four aerosol types. White dashed lines indicate discontinuous intervals, as the data cover nighttime periods only.

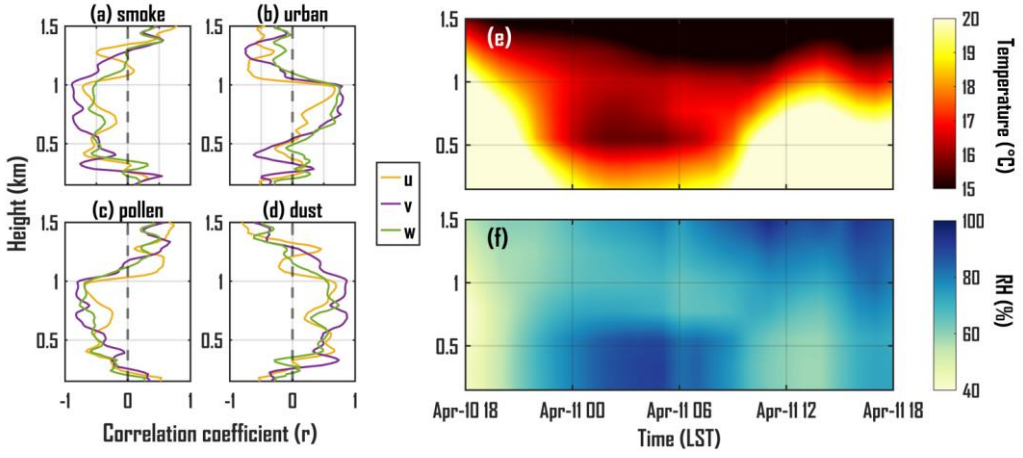

Figure 10: Data from April 10 to 11, 2023: (a–d) correlation coefficients between wind speed components and the contributions of four aerosol types to β_R; (e) temperature and (f) relative humidity from ERA5 reanalysis.

4. Conclusions

To achieve refined vertical profiling of tropospheric aerosols, this study utilizes the multi-wavelength Mie-Raman-fluorescence lidar system at the Atmospheric Boundary Layer Eco-Environment Shanghuang Observatory to propose an improved algorithm that classifies aerosols into four categories: smoke, urban, pollen, and dust. This method is based on a seven-parameter synergistic constraint, including fluorescence capacity, dual-wavelength particle depolarization ratios, dual-

https://doi.org/10.5194/egusphere-2026-2017
Preprint. Discussion started: 29 April 2026

wavelength lidar ratios, and Ångström exponents corresponding to dual-wavelength color ratios. By integrating Monte Carlo stochastic simulation with the least squares method, the algorithm effectively mitigates the limitations arising from the use of limited parameters in complex mixed scenarios, achieving a quantitative decomposition of the 532 nm backscatter coefficients and mass concentrations for these four aerosol types. Comparisons with multi-source observational data validate the rationality and reliability of the proposed method. Regarding vertical distribution, the 532 nm backscatter coefficients retrieved from the Raman channel show high consistency in both magnitude and vertical structure with CALIPSO satellite overpass observations. Similarly, bioaerosol concentrations retrieved from the fluorescence channel demonstrate magnitude consistency and structural continuity with UAV aerial survey results. In the near-surface layer, the retrieved mass concentrations of $PM_{2.5}$ (smoke and urban) and PM_{10} (pollen and dust) agree well with in situ monitoring results, achieving the highest accuracy under winter low-loading background conditions. Furthermore, the multi-parameter constraint effectively corrects the overestimation of urban aerosols caused by high relative humidity (RH) and the underestimation of near-surface pollen, further demonstrating the reliability of the multi-constraint retrieval method.

Sensitivity analysis conducted in this study provides in-depth insights into the physical robustness and spatiotemporal response characteristics of the multi-parameter constraint mechanism. Fluorescence capacity, owing to its non-overlapping values, serves as the most robust constraint for differentiating aerosol types. In contrast, the sensitivity of other parameters reflects complex microphysical coupling mechanisms. The depolarization ratio (*PDR*) is primarily controlled by the signal-to-noise ratio and particle morphology; near-surface pollen in spring exhibits high sensitivity to PDR_{355} perturbations due to suppression by the strong Rayleigh scattering background, while urban aerosols in the upper boundary layer during summer and autumn show increased uncertainty. This is primarily driven by the 'spherical-nonspherical' phase transition induced by elevated relative humidity and hygroscopic growth near the boundary layer top. Variations in the Ångström exponent (*BÅE*) reveal the evolution of particle size distributions and spectral properties. Aged smoke exhibits the lowest sensitivity because its accumulation mode is highly homogenized, whereas pollen shows a flattened spectral dependence at longer wavelengths as it enters the geometric optics regime, retaining microstructural sensitivity primarily in the UV band and thus exhibiting higher sensitivity to $BÅE_{355/532}$ perturbations. Furthermore, the lidar ratio (*LR*) highlights the shift in the "absorption-scattering" competition mechanism. Seasonally, this manifests as a transition from LR_{355} sensitivity dominated by strong absorbing components in spring and winter to LR_{532} sensitivity dominated by hygroscopic scattering enhancement in summer and autumn. Vertically, the sensitivity of urban aerosols to LR_{355} decreases with altitude, effectively verifying the UV absorption decay process caused by aging and coating.

Case studies validated the algorithm's capability to accurately resolve the vertical evolution of aerosols in complex atmospheric environments, effectively distinguishing meteorologically driven optical variations from fluctuations in aerosol mass concentration. Regarding the transport-deposition events of spring dust and pollen, the algorithm not only confirmed the joint control mechanism of advection transport and local inversion stratification by capturing the wedge-shaped settling dynamics of aerosol layers but also accurately identified pollutant mass outbreaks driven by the combined effects of hygroscopic growth and boundary layer accumulation in high-humidity environments. Furthermore, the strong scattering contribution of smoke in

https://doi.org/10.5194/egusphere-2026-2017
Preprint. Discussion started: 29 April 2026

autumn demonstrated the advantage of the algorithm in handling low mass loading scenarios, providing a reliable physical basis for precisely quantifying the radiative forcing effects of invisible aerosol layers in complex atmospheric backgrounds. In summary, this study provides a viable technical route for high spatiotemporal resolution aerosol classification using multi-wavelength Mie-Raman-fluorescence lidar, holding significant scientific importance for improving regional air quality forecasting accuracy and assessing aerosol climate effects.

Data availability

The data in this study are available from the authors upon request (tingyang@mail.iap.ac.cn).

Supplement link

The link to the supplement will be included by Copernicus, if applicable.

Author contributions

YT drafted the manuscript. TY provided scientific guidance, supervised the study and revised the manuscript. ZW contributed to manuscript review. YT participated in manuscript revision. LZ contributed to data collection and organization. WL, QX, TW, and SK provided the instruments and technical support. All authors reviewed and revised this paper.

Competing interests

The authors declare that they have no conflict of interest.

Disclaimer

Publisher's note: Copernicus Publications remains neutral with regard to jurisdictional claims made in the text, published maps, institutional affiliations, or any other geographical representation in this paper. While Copernicus Publications makes every effort to include appropriate place names, the final responsibility lies with the authors.

Acknowledgements

We thank for the technical support of the National large Scientific and Technological Infrastructure "Earth System Numerical Simulation Facility" (https://cstr.cn/31134.02.EL, last access: 10 January 2026). Ting Yang would like to express gratitude towards the Program of the Youth Innovation Promotion Association (CAS).

https://doi.org/10.5194/egusphere-2026-2017
Preprint. Discussion started: 29 April 2026

Financial support

This research has been supported by the National Natural Science Foundation of China (NSFC) Excellent Young Scientists Fund (grant no. 42422506), National Key Research and Development Program of China (grant no. 2023YFC3705801) and the National Natural Science Foundation of China (grant no. 42275122).

Review statement

The review statement will be added by Copernicus Publications listing the handling editor as well as all contributing referees according to their status anonymous or identified.

References

Ahmad, M., Ahmad, M., Alam, K., Zeb, B., Khan, K., and Ditta, A.: Large increase in anthropogenic emissions in an urban environment and their associated air quality implications, Environmental Monitoring and Assessment, 197, 1055, 10.1007/s10661-025-14518-0, 2025.

Akinyoola, J. A., Oluleye, A., and Gbode, I. E.: A Review of Atmospheric Aerosol Impacts on Regional Extreme Weather and Climate Events, Aerosol Science and Engineering, 8, 249-274, 10.1007/s41810-024-00223-x, 2024.

Bohlmann, S., Shang, X., Vakkari, V., Giannakaki, E., Leskinen, A., Lehtinen, K. E. J., Pätsi, S., and Komppula, M.: Lidar depolarization ratio of atmospheric pollen at multiple wavelengths, Atmos. Chem. Phys., 21, 7083-7097, 10.5194/acp-21-7083-2021, 2021.

Chen, X., Yang, T., Wang, H., Wang, F., and Wang, Z.: Variations and drivers of aerosol vertical characterization after clean air policy in China based on 7-years consecutive observations, Journal of Environmental Sciences, 125, 499-512, https://doi.org/10.1016/j.jes.2022.02.036, 2023.

Cheng, Y., Kong, Z., Yu, J., and Mei, L.: Measurements of the single-wavelength aerosol Ångström exponent based on differential absorption, Optics & Laser Technology, 184, 112437, https://doi.org/10.1016/j.optlastec.2025.112437, 2025.

Chiang, T.-Y., Chen, W.-N., Chou, C. C. K., Chang, S.-Y., and Wu, T.-S.: Effects of boundary layer variations on physicochemical characteristics of aerosols in mid-low-altitude regions, Science of The Total Environment, 904, 166849, https://doi.org/10.1016/j.scitotenv.2023.166849, 2023.

Fernald, F. G.: Analysis of atmospheric lidar observations: some comments, Appl. Opt., 23 5, 652, 1984.

Filioglou, M., Tiitta, P., Shang, X., Leskinen, A., Ahola, P., Pätsi, S., Saarto, A., Vakkari, V., Isopahkala, U., and Komppula, M.: Lidar estimates of birch pollen number, mass, and CCN-related concentrations, Atmos. Chem. Phys., 25, 1639-1657, 10.5194/acp-25-1639-2025, 2025.

Fu, Y., Lin, Q., Zhang, G., Yang, Y., Yang, Y., Lian, X., Peng, L., Jiang, F., Bi, X., Li, L., Wang, Y., Chen, D., Ou, J., Wang, X., Peng, P., Zhu, J., and Sheng, G.: Impact of in-cloud aqueous processes on the chemical compositions and morphology of individual atmospheric aerosols, Atmos. Chem. Phys., 20, 14063-14075, 10.5194/acp-20-14063-2020, 2020.

Gast, B., Jimenez, C., Ansmann, A., Haarig, M., Engelmann, R., Fritzsch, F., Floutsi, A. A., Griesche, H., Ohneiser, K., Hofer, J., Radenz, M., Baars, H., Seifert, P., and Wandinger, U.: Invisible aerosol layers: improved lidar detection capabilities by means of laser-induced aerosol fluorescence, Atmos. Chem. Phys., 25, 3995-4011, 10.5194/acp-25-3995-2025, 2025.

Gui, L., Tao, M., Wang, Y., Wang, L., Chen, L., Lin, C., Tao, J., Wang, J., and Yu, C.: Climatology of aerosol types and their vertical distribution over East Asia based on CALIPSO lidar measurements, International Journal of Climatology, 42, 6042-6054, https://doi.org/10.1002/joc.7599, 2022.

Haarig, M., Engelmann, R., Baars, H., Gast, B., Althausen, D., and Ansmann, A.: Discussion of the spectral slope of the lidar ratio between 355 and 1064 nm from multiwavelength Raman lidar observations, Atmos. Chem. Phys., 25, 7741-7763, 10.5194/acp-25-7741-2025, 2025.

https://doi.org/10.5194/egusphere-2026-2017
Preprint. Discussion started: 29 April 2026

Haarig, M., Ansmann, A., Engelmann, R., Baars, H., Toledano, C., Torres, B., Althausen, D., Radenz, M., and Wandinger, U.: First triple-wavelength lidar observations of depolarization and extinction-to-backscatter ratios of Saharan dust, Atmos. Chem. Phys., 22, 355-369, 10.5194/acp-22-355-2022, 2022.

Huang, Z., Wang, Y., Zhou, T., Ji, Y., Bi, J., Shi, J., Wen, H., and Huang, J.: Raman-Polarization-Fluorescence Spectroscopic Lidar for Real-Time Detection of Humic-like Substance Profiles, Environmental Science & Technology, 59, 7235-7245, 10.1021/acs.est.5c00028, 2025.

Ito, A., Adebiyi, A. A., Huang, Y., and Kok, J. F.: Less atmospheric radiative heating by dust due to the synergy of coarser size and aspherical shape, Atmos. Chem. Phys., 21, 16869-16891, 10.5194/acp-21-16869-2021, 2021.

Jiang, Y., Yang, H., Tan, W., Chen, S., Chen, H., Guo, P., Xu, Q., Gong, J., and Yu, Y.: Observation and Classification of Low-Altitude Haze Aerosols Using Fluorescence–Raman–Mie Polarization Lidar in Beijing during Spring 2024, 10.3390/rs16173225, 2024.

Levy Ii, H., Horowitz, L. W., Schwarzkopf, M. D., Ming, Y., Golaz, J.-C., Naik, V., and Ramaswamy, V.: The roles of aerosol direct and indirect effects in past and future climate change, Journal of Geophysical Research: Atmospheres, 118, 4521-4532, https://doi.org/10.1002/jgrd.50192, 2013.

Li, J., Carlson, B. E., Yung, Y. L., Lv, D., Hansen, J., Penner, J. E., Liao, H., Ramaswamy, V., Kahn, R. A., Zhang, P., Dubovik, O., Ding, A., Lacis, A. A., Zhang, L., and Dong, Y.: Scattering and absorbing aerosols in the climate system, Nature Reviews Earth & Environment, 3, 363-379, 10.1038/s43017-022-00296-7, 2022.

Li, L., Li, M., Fan, X., Chen, Y., Lin, Z., Hou, A., Zhang, S., Zheng, R., and Chen, J.: Measurement report: The variation properties of aerosol hygroscopic growth related to chemical composition during new particle formation days in a coastal city of Southeast China, Atmos. Chem. Phys., 25, 3669-3685, 10.5194/acp-25-3669-2025, 2025.

Li, M., Cao, X., Zhang, Z., Ji, H., Zhang, M., Guo, Y., Tian, P., and Liang, J.: Optical Properties and Vertical Distribution of Aerosols Using Polarization Lidar and Sun Photometer over Lanzhou Suburb in Northwest China, Remote Sensing, 15, 4927, 2023.

Matthews, B. H., Alsante, A. N., and Brooks, S. D.: Pollen Emissions of Subpollen Particles and Ice Nucleating Particles, ACS Earth Space Chem, 7, 1207-1218, 10.1021/acsearthspacechem.3c00014, 2023.

Milousis, A., Klingmüller, K., Tsimpidi, A. P., Kok, J. F., Kanakidou, M., Nenes, A., and Karydis, V. A.: Impact of mineral dust on the global nitrate aerosol direct and indirect radiative effect, Atmos. Chem. Phys., 25, 1333-1351, 10.5194/acp-25-1333-2025, 2025.

Miri, R., Pujol, O., Hu, Q., Goloub, P., Veselovskii, I., Podvin, T., and Ducos, F.: Innovative aerosol hygroscopic growth study from Mie–Raman–fluorescence lidar and microwave radiometer synergy, Atmos. Meas. Tech., 17, 3367-3375, 10.5194/amt-17-3367-2024, 2024.

Mylonaki, M., Papayannis, A., Anagnou, D., Veselovskii, I., Papanikolaou, C.-A., Kokkalis, P., Soupiona, O., Foskinis, R., Gidarakou, M., and Kralli, E.: Optical and Microphysical Properties of Aged Biomass Burning Aerosols and Mixtures, Based on 9-Year Multiwavelength Raman Lidar Observations in Athens, Greece, 10.3390/rs13193877, 2021.

Ortiz-Amezcua, P., Bedoya-Velásquez, A. E., Benavent-Oltra, J. A., Pérez-Ramírez, D., Veselovskii, I., Castro-Santiago, M., Bravo-Aranda, J. A., Guedes, A., Guerrero-Rascado, J. L., and Alados-Arboledas, L.: Implementation of UV rotational Raman channel to improve aerosol retrievals from multiwavelength lidar, Opt. Express, 28, 8156-8168, 10.1364/OE.383441, 2020.

Pan, X., Chin, M., Kahn, R. A., Matsui, H., Takemura, T., Lin, M., Xie, Y., Kim, D., and Val Martin, M.: The sensitivity of smoke aerosol dispersion to smoke injection height and source-strength: a multi-model AeroCom study, Atmos. Chem. Phys., 26, 171-196, 10.5194/acp-26-171-2026, 2026.

Peterson, D. A., Campbell, J. R., Hyer, E. J., Fromm, M. D., Kablick, G. P., Cossuth, J. H., and DeLand, M. T.: Wildfire-driven thunderstorms cause a volcano-like stratospheric injection of smoke, npj Climate and Atmospheric Science, 1, 30, 10.1038/s41612-018-0039-3, 2018.

Prank, M., Tonttila, J., Shang, X., Romakkaniemi, S., and Raatikainen, T.: Can pollen affect precipitation?, Atmos. Chem. Phys., 25, 183-197, 10.5194/acp-25-183-2025, 2025.

Quaas, J., Arola, A., Cairns, B., Christensen, M., Deneke, H., Ekman, A. M. L., Feingold, G., Fridlind, A., Gryspeerdt, E., Hasekamp, O., Li, Z., Lipponen, A., Ma, P. L., Mülmenstädt, J., Nenes, A., Penner, J. E., Rosenfeld, D., Schrödner, R., Sinclair, K., Sourdeval, O., Stier, P., Tesche, M., van Diedenhoven, B., and Wendisch, M.: Constraining the Twomey effect from satellite observations: issues and perspectives, Atmos. Chem. Phys., 20, 15079-15099, 10.5194/acp-20-15079-2020, 2020.

https://doi.org/10.5194/egusphere-2026-2017
Preprint. Discussion started: 29 April 2026

Rajesh, T. A. and Ramachandran, S.: Extensive and intensive properties of aerosol over distinct environments: Influence of anthropogenic emissions and meteorology, Journal of Atmospheric and Solar-Terrestrial Physics, 202, 105223, https://doi.org/10.1016/j.jastp.2020.105223, 2020.

Rao, Z., He, T., Hua, D., Wang, Y., Wang, X., Chen, Y., and Le, J.: Preliminary measurements of fluorescent aerosol number concentrations using a laser-induced fluorescence lidar, Appl. Opt., 57, 7211-7215, 10.1364/AO.57.007211, 2018.

Reddy, K. R. O., Zhang, X., and Bi, L.: Seasonal aerosol variations over a coastal city, Zhoushan, China from CALIPSO observations, Atmospheric Research, 218, 117-128, 2019.

Schuster, G. L., Vaughan, M., MacDonnell, D., Su, W., Winker, D., Dubovik, O., Lapyonok, T., and Trepte, C.: Comparison of CALIPSO aerosol optical depth retrievals to AERONET measurements, and a climatology for the lidar ratio of dust, Atmos. Chem. Phys., 12, 7431-7452, 10.5194/acp-12-7431-2012, 2012.

Singh, N., Solanki, R., Ojha, N., Janssen, R. H. H., Pozzer, A., and Dhaka, S. K.: Boundary layer evolution over the central Himalayas from radio wind profiler and model simulations, Atmos. Chem. Phys., 16, 10559-10572, 10.5194/acp-16-10559-2016, 2016.

Solanki, R., Guo, J., Li, J., Singh, N., Guo, X., Han, Y., Lv, Y., Zhang, J., and Liu, B.: Atmospheric-Boundary-Layer-Height Variation over Mountainous and Urban Sites in Beijing as Derived from Radar Wind-Profiler Measurements, Boundary-Layer Meteorology, 181, 125-144, 10.1007/s10546-021-00639-9, 2021.

Veselovskii, I., Hu, Q., Goloub, P., Podvin, T., Barchunov, B., and Korenskii, M.: Combining Mie–Raman and fluorescence observations: a step forward in aerosol classification with lidar technology, Atmos. Meas. Tech., 15, 4881-4900, 10.5194/amt-15-4881-2022, 2022.

Veselovskii, I., Hu, Q., Goloub, P., Podvin, T., Dubois, G., Kolgotin, A., and Korenskii, M.: Impact of water uptake on fluorescence of atmospheric aerosols: insights from Mie–Raman–fluorescence lidar measurements, Atmos. Meas. Tech., 18, 6039-6051, 10.5194/amt-18-6039-2025, 2025.

Veselovskii, I., Kasianik, N., Korenskii, M., Hu, Q., Goloub, P., Podvin, T., and Liu, D.: Multiwavelength fluorescence lidar observations of smoke plumes, Atmos. Meas. Tech., 16, 2055-2065, 10.5194/amt-16-2055-2023, 2023.

Veselovskii, I., Hu, Q., Goloub, P., Podvin, T., Korenskiy, M., Pujol, O., Dubovik, O., and Lopatin, A.: Combined use of Mie–Raman and fluorescence lidar observations for improving aerosol characterization: feasibility experiment, Atmos. Meas. Tech., 13, 6691-6701, 10.5194/amt-13-6691-2020, 2020.

Veselovskii, I., Barchunov, B., Hu, Q., Goloub, P., Podvin, T., Korenskii, M., Dubois, G., Boissiere, W., and Kasianik, N.: Retrieval and analysis of the composition of an aerosol mixture through Mie–Raman–fluorescence lidar observations, Atmos. Meas. Tech., 17, 4137-4152, 10.5194/amt-17-4137-2024, 2024.

Wang, L., Mačak, M. B., Stanič, S., Bergant, K., Gregorič, A., Drinovec, L., Močnik, G., Yin, Z., Yi, Y., Müller, D., and Wang, X.: Investigation of Aerosol Types and Vertical Distributions Using Polarization Raman Lidar over Vipava Valley, 10.3390/rs14143482, 2022.

Wang, Y.: Aerosol Effects on the Atmosphere: Types, Mechanisms and Future Perspectives, E3S Web Conf., 606, 03006, 2025.

Wang, Z., Pan, X., Sun, Y., Xin, J., Su, H., Cao, J., Li, J., Yang, T., Liu, H., Yao, W., Xu, W., Chen, X., Zhou, W., Ma, Y., Cheng, X., Ye, J., Hu, B., Jiang, R., Wang, Z., Ge, B., Wu, L., Li, X., Li, J., Wu, Z., Kong, L., Zhu, M., Jia, J., Li, X., Fang, X., and Liu, L.: Atmospheric Boundary Layer Eco-Environment Shanghuang Observatory: An Integrated Multiscale Research Platform in Southeastern China for Understanding Boundary Layer Processes, Atmospheric Chemistry Feedback, and Extreme Weather–Climate Linkages, Advances in Atmospheric Sciences, 10.1007/s00376-025-5307-7, 2025.

Wise, M. E., Semeniuk, T. A., Bruintjes, R., Martin, S. T., Russell, L. M., and Buseck, P. R.: Hygroscopic behavior of NaCl-bearing natural aerosol particles using environmental transmission electron microscopy, Journal of Geophysical Research: Atmospheres, 112, https://doi.org/10.1029/2006JD007678, 2007.

Young, L. H., Hsiao, T. C., Griffith, S. M., Huang, Y. H., Hsieh, H. G., Lin, T. H., Tsay, S. C., Lin, Y. J., Lai, K. L., Lin, N. H., and Lin, W. Y.: Secondary inorganic aerosol chemistry and its impact on atmospheric visibility over an ammonia-rich urban area in Central Taiwan, Environ Pollut, 312, 119951, 10.1016/j.envpol.2022.119951, 2022.

Yu, P., Toon, O. B., Bardeen, C. G., Zhu, Y., Rosenlof, K. H., Portmann, R. W., Thornberry, T. D., Gao, R.-S., Davis, S. M., Wolf, E. T., de Gouw, J., Peterson, D. A., Fromm, M. D., and Robock, A.: Black carbon lofts wildfire smoke high into the stratosphere to form a persistent plume, Science, 365, 587-590, doi:10.1126/science.aax1748, 2019.

https://doi.org/10.5194/egusphere-2026-2017
Preprint. Discussion started: 29 April 2026

Zhang, D., Martin, R. V., Liu, X., van Donkelaar, A., Oxford, C. R., Li, Y., Meng, J., Leung, D. M., Kok, J. F., Li, L., Zhu, H., Turner, J. R., Yan, Y., Brauer, M., Rudich, Y., and Windwer, E.: Improving annual fine mineral dust representation from the surface to the column in GEOS-Chem 14.4.1, Geosci. Model Dev., 18, 6767-6803, 10.5194/gmd-18-6767-2025, 2025.

Zhao, Y., Wang, X., Cai, Y., Pan, J., Yue, W., Xu, H., and Wang, J.: Measurements of atmospheric aerosol hygroscopic growth based on multi-channel Raman-Mie lidar, Atmospheric Environment, 246, 118076, https://doi.org/10.1016/j.atmosenv.2020.118076, 2021.